Interactively Cutting and Constraining Vertices in Meshes Using Augmented Matrices

YU-HONG YEUNG
Purdue University
and
JESSICA CROUCH
Old Dominion University
and
ALEX POTHEN
Purdue University

We present a finite element solution method that is well-suited for interactive simulations of cutting meshes in the regime of linear elastic models. Our approach features fast updates to the solution of the stiffness system of equations to account for real-time changes in mesh connectivity and boundary conditions. Updates are accomplished by augmenting the stiffness matrix to keep it consistent with the changes to the underlying model, without re-factoring the matrix at each step of cutting. The initial stiffness matrix and its Cholesky factors are used to implicitly form and solve a Schur complement system using an iterative solver. As changes accumulate over many simulation time steps, the augmented solution method slows down due to the size of the augmented matrix. However, by periodically re-factoring the stiffness matrix in a concurrent background process, fresh Cholesky factors that incorporate recent model changes can replace the initial factors. This controls the size of the augmented matrices and provides a way to maintain a fast solution rate as the number of changes to a model grows. We exploit sparsity in the stiffness matrix, the right-hand-side vectors and the solution vectors to compute the solutions fast, and show that the time complexity of the update steps is bounded linearly by the size of the Cholesky factor of the initial matrix. Our complexity analysis and experimental results demonstrate that this approach scales well with problem size. Results for cutting and deformation of 3D linear elastic models are reported for meshes representing the brain, eye, and model problems with element counts up to $167,000$; these show the potential of this method for real-time interactivity. An application to limbal incisions for surgical correction of astigmatism, where linear elastic models and small deformations are sufficient, is included.

Categories and Subject Descriptors: I.3.5 [**Computer Graphics**]: Computational Geometry and Object Modeling—*Physically based modeling*; I.6.3 [**Simulation and Modeling**]: Applications; I.1.2 [**Symbolic and Algebraic Manipulation**]: Algorithms—*Algebraic algorithms*

Additional Key Words and Phrases: finite element, surgery simulation, real-time, deformable model, cutting.

1. INTRODUCTION

A method to support interactively cutting or deforming solid finite element models by solving the time-varying equations quickly is presented in this paper. Topological mesh modifications and boundary condition changes are essential parts of many simulation scenarios, particularly surgical simulations. Integrating support for cutting with real-time finite element solution methods is a computational challenge, first because graphic and haptic rendering require demanding update rates, and second because connectivity changes due to cutting necessitate corresponding changes to the underlying matrix equations. Such changes invalidate previous factorizations or inverse computations for the stiffness matrix, requiring either computationally expensive update procedures or solution via an iterative method.

Many simulations that involve cutting would ideally support unpredictable cutting paths. Enabling unpredictable cutting can require that the internal deformation of a solid model be computed and tracked so that accurate cut surfaces are exposed as cuts progress into a model's potentially inhomogeneous interior. Thus a desirable solution method would quickly compute the displacement of all nodes in a 3D mesh while accommodating changes to the mesh and equations due to cutting, variable pushing and pulling forces, and changes to the fixed displacements (Dirichlet boundary conditions) created by different fixation scenarios.

Our solution approach is to represent the changing mesh of a linear elastic model with an augmented 2 by 2 block matrix in which the (1,1) block is fixed, the (2,2) block is zero, and the other blocks vary. We then use an implicit solution approach to the Schur complement system, in which we exploit the sparsity of the matrices involved. Our current solution approach combines a matrix-factorization based method for the (1,1) block with a Krylov space-

We acknowledge support from DOE grant 13SC-003242, NSF grants CCF-1218916 and CCF-1552323, and the Purdue Research Foundation.
Authors' addresses: Y.-H. Yeung, A. Pothen, Department of Computer Science, Purdue University, West Lafayette IN 47907 {yyeung|apothen}@cs.purdue.edu; J. Crouch, Department of Computer Science, Old Dominion University, Norfolk VA 23529 jrcrouch@cs.odu.edu.

DOI:http://dx.doi.org/10.1145/XXXXXXX.YYYYYYY

based iterative solver for the Schur complement. A detailed treatment of the algorithm's complexity shows that performance scales well with model size while supporting arbitrary cutting of any valid finite element mesh. Periodic re-factorizations of the stiffness matrix are performed concurrently with the real-time solution loop so that changes to the model eventually become directly incorporated into the non-augmented stiffness matrix factors. This allows the list of nodes affected by accumulated changes to be periodically reduced, limiting the growth in solution time that can occur as the list of mesh modifications grows longer over time.

A variety of existing algorithms for mesh generation [Goksel and Salcudean 2011] [Mohamed and Davatzikos 2004] [Lederman et al. 2010], collision detection [Teschner et al. 2005] [Spillmann and Harders 2012] [Zhang and Kim 2012], and mesh refinement [Steinemann et al. 2006] [Mor and Kanade 2000] [Forest et al. 2002] are available. Such algorithms that work for finite element models can be paired with our solution algorithm to construct a simulation platform. Thus the scope of this paper does not include algorithms for simulation tasks other than solving the finite element system of equations. In addition, although only node cutting is demonstrated in this paper, many cutting and remeshing algorithms cut edges and surfaces, and these can also be solved using our method. A feature of the solution algorithm presented is its flexibility to work with structured and unstructured meshes as well as a number of different methods for adapting mesh geometry to respect a cut surface.

Our results show that the augmented approach works well on linear models exhibiting small deformations. This is valuable for the important subset of medical applications that involve small magnitude but medically significant deformations. For these applications linear elasticity can be an appropriate material model because it realistically simulates deformation at a lower computational cost than more complex models. A variety of simulation results have been published based on linear elastic models in both the computer graphics and biomedical engineering literature, in many cases with validation of model accuracy against empirical data derived from medical images or mechanical experiments. Examples include modeling the lens [Mikielewicz et al. 2013] and cornea [Gefen et al. 2009] of the eye, prostate biopsy [Jahya et al. 2014] and prostate brachytherapy [Crouch et al. 2007], and bone [Keaveny et al. 1994] [Andreaus et al. 2014] [Juszczyk et al. 2011]. We recognize that linear elasticity will not adequately model these organs and tissue types under all loading scenarios, but the community has found the linear elastic model to be useful for biomechanical modeling when limited forces are applied. Non-linear models are not considered in this paper but will be investigated in the future.

1.1 Our Contributions

The three main contributions of this work are:

—a unified augmented matrix formulation of a finite element model that allows both continuous, unpredictable cutting, and imposition of new boundary conditions. This formulation keeps the original stiffness matrix as a submatrix to eliminate the necessity of re-factorization at each timestep.

—a hybrid solution approach that utilizes a direct solver and an iterative solver. The solution of the updated portion of a mesh is decoupled from the solution of the unchanged portion, facilitating fast updates when the percentage of mesh elements affected by topological changes is small. Preconditioning techniques for the iterative part of the solution method are also discussed.

—acceleration of the solution algorithms by exploiting sparsity in both the matrices and the vectors. A complexity analysis is presented using graph theory concepts applied to the accelerated solution method.

1.2 Article Organization

This paper is organized as follows. Section 2 reviews previous work on the real-time solution of physics-based models and finite element equations. Section 3 presents our new augmented method for assembling a finite element system of equations and accounting for changes in mesh connectivity and boundary conditions via updates to stiffness matrix factors. Section 4 presents speed and accuracy results from finite element deformation and cutting experiments with models of various size. Finally, Section 5 discusses conclusions and directions for future work.

2. PREVIOUS WORK

Beginning with Terzopoulos et al. [1987] [Terzopoulos and Fleischer 1988], physics-based deformable models have been used for animation and simulation. By the mid-1990's, a variety of work specific to surgery simulation began to appear [Cover et al. 1993] [Bro-Nielsen and Cotin 1996]. This section reviews existing approaches for computing physics-based deformation solutions, with a particular focus on methods that involve finite element analysis and cutting. Methods are categorized according to whether they use a direct solution approach with pre-computation, an iterative solver, or a combination of both.

2.1 Pre-computation Approaches

Pre-computation strategies accelerate the solution step of a simulation by shifting the bulk of the computational burden to a preprocessing stage. The bottleneck in a finite element simulation is the solution of a system of linear equations, $Ka = f$, where K is the stiffness matrix, a is a vector of nodal displacements, and f is a vector of nodal forces. Precomputation methods such as [Zhong et al. 2005] minimize the time required to calculate the solution vector by inverting K before a simulation begins so that a can be directly computed via the multiplication $a = K^{-1}f$ during the simulation. Since K^{-1} is dense, condensation methods such as [Bro-Nielsen and Cotin 1996], [Bro-Nielsen 1998], [Berkley et al. 2004], and [Lee et al. 2010] further reduce computation time by producing from the full inverse matrix a smaller dimension one that contains only the equations necessary to compute a solution for a small subset of the nodes, such as a set of surface nodes. The inability to compute a solution for nodes not included in the pre-selected subset poses a problem for applications that involve cutting. The Sherman-Morrison-Woodbury update formula [Hager 1989] has been used to address this by allowing selected degrees of freedom to be added back into a condensed stiffness matrix as they are needed. This approach was suggested by James and Pai [1999], and later was used in needle insertion simulation [DiMaio and Salcudean 2002] and [DiMaio 2003], and in a cutting simulation [Zhong et al. 2005]. The approach is most successful when access to a small number of degrees of freedom needs to be added to an already condensed system. It becomes computationally intensive and slow as the added number of degrees of freedom increases and is impractical for applications that require cutting with non-trivial remeshing.

A variation on the precomputed inverse approach sharing some similarities with our work is the precomputed stiffness matrix factorization described by Turkiyyah [2011] which updated a Cholesky factorization to accommodate the addition and modification of discontinuous basis functions along a cutting path. While our work also updates the solution to a system of equations involving the stiffness matrix, it does so without updating the factors by solving a Schur complement system with an iterative solver. Hence our method supports *any* local mesh modification, whether from remeshing or addition of basis functions; consequently our method's update process substantially differs from Turkiyyah's work.

Solution techniques that rely on the superposition principle such as [Cotin et al. 1999], [Picinbono et al. 2002], and [Sedef et al. 2006] pre-compute and record the set of node displacements that result from a constraint being applied to a single node. This computation is repeated for every node that might be subject to a constraint, and all the results are stored. At runtime nodal displacements are computed as a linear combination of the stored results. For some applications this approach can closely approximate the ideal solution, but without modification it cannot handle changes in mesh connectivity.

Pre-computed Green's functions have also been used by Nikitin et al., [2002] and James and Pai [2003] to quickly compute deformation solutions for subsets of mesh nodes. Similarly, the banded matrix method proposed by Berkley et al. [1999] prioritizes and rearranges the rows and columns of a stiffness matrix based on node type, then factors the stiffness matrix in such a way that a fast update is provided only for the highest priority nodes. In both cases, solutions for internal nodes are generally not computed.

A limitation generally shared by pre-computation approaches is that results produced in the pre-computation phase are invalidated when the topology of the mesh changes, so cutting and remeshing require special consideration. Constraint removal is a pre-computation approach that requires cutting paths to be known a priori. Lindblad and Turkiyyah [2007] and Sela et al. [2007] have demonstrated how duplicate nodes along a cutting path can be constrained to move together until they are cut, at which time the constraint is removed to open up a predefined cut.

Discontinuous basis functions provide a more flexible cutting scheme that has been used in concert with pre-computation. This approach was originally introduced in the engineering literature as a way of studying crack formation [Mos et al. 1999] and more recently has been applied to the problem of cutting in surgical simulations [Vigneron et al. 2004] [Turkiyyah et al. 2011]. Unpredictable and arbitrary cutting paths are accommodated through the addition of new degrees of freedom that use discontinuous interpolation functions to account for mid-element breaks in nodal influence. The Turkiyyah work has important similarities to our work, in that both approaches progressively update the solution of the stiffness matrix equation. However, an important distinction is that our work maintains a finite element mesh that respects cut surfaces by remeshing areas as needed, while the Turkiyyah work maintains separate, distinct meshes for graphic rendering and for computation of the finite element solution. In their method rendered surfaces are remeshed as needed but the finite element equations accommodate cutting through the addition of discontinuous basis functions without remeshing. As shown in [Lindblad and Turkiyyah 2007], an update procedure similar to the Sherman-Morrison-Woodbury update can be employed to update a pre-computed inverse stiffness matrix to account for the new degrees of freedom. Because the complexity of Sherman-Morrison-Woodbury update is cubic with respect to the number of matrix rows and columns changed, this works well only when the modifications are very limited.

Nonlinear elastodynamics problems in which the nonlinearities are due to rotations within an object have been solved using a corotational approach in [Hecht et al. 2012]. They approximate the rotation by applying an average of the rotations of the surrounding elements to a node. They compute the solution by updating the Cholesky factors of the system matrix by exploiting the nonzero pattern of the factor due to a nested dissection ordering, observing as we have done here that only the submatrices of the factor that lie on a path in the elimination tree from a submatrix to the root of the tree are affected. In order to have the simulations run fast, they trade-off an increased error tolerance for time, by choosing which submatrices in the factors to update. There are major differences between our work and theirs. They have applied their work to nonlinear problems where rotations are the major source of the non-linearity, while our work in this paper applies to linear problems. Our augmented matrix approach models the stiffness system exactly and the solutions should be identical to the original system in exact arithmetic. They have not applied their work to cutting problems addressed in this work, and it would require the ability to handle changes in the mesh topology. The way the two approaches exploit sparsity is also different. Hecht et al. have chosen to update selected submatrices of the Cholesky factors, and this requires dynamic updates to the large datastructure that stores the Cholesky factor and the update matrices, increasing the storage needs. Our approach is to update the solution but not the Cholesky factors, by *implicitly* solving a Schur complement system with a Krylov space solver, without forming the Schur complement matrix. We exploit the sparsity not only in the factor, but also in the right-hand-side vectors and the solutions, as described in Sec. 3.3 and the Appendix. The time complexity of the update step is bounded linearly by the number of nonzeros in the (static) Cholesky factor (and the number of iterations of the Krylov space solver) in our case, but the corotational approach cannot be bounded in this manner since the factors are updated.

Finally we consider the CHOLMOD approach of Chen, Davis and Hager [2008] for updating the Cholesky factors when rows or columns are added or deleted from the matrix. This algorithm relies on dynamic supernodal updates of the Cholesky factor. Unfortunately the number of columns to be added or deleted (change in the rank of the factor) during the cutting of meshes is much larger than can be efficiently performed with this software since we need to remesh around the cut. Hecht et al. [2012] have come to similar conclusions for their problem. Furthermore, dynamic updates to the large sparse Cholesky factor and update matrix data structure are expensive, and instead we work with an implicit Schur complement approach whose time complexity can be bounded linearly by the size of the Cholesky factor.

2.2 Iterative Solvers

Iterative solvers do not share the same limitations as pre-computation methods because all of the calculations needed to produce a solution occur at runtime. Thus iterative solvers can be successfully applied when stiffness matrix updates are caused by topological mesh changes. However, using an iterative solver does require that attention be paid to issues of convergence and stability.

Conjugate Gradient solvers have been frequently used with finite element simulations [Frank et al. 2001] [Nienhuys and van der Stappen 2001] [Courtecuisse et al. 2010]. The popularity and relatively straightforward implementation of the Conjugate Gradient algorithm make the method a good benchmark for comparisons with alternative solution methods. Conjugate Gradient implementations that take advantage of sparse matrix-vector multiplication have been used for interactive applications and can be accelerated with parallel [Chentanez et al. 2009] and GPU implementations [Wu and Heng 2004]. However, the simulation community continues to seek solution methods that outperform Conjugate Gradient, as real-time performance on higher resolution models promises improved realism.

Some of the most recent work in interactive finite element simulation has explored the use of multigrid solution methods [Dick et al. 2011a] [Zhu et al. 2010] [Georgii and Westermann 2006] [Wu and Tendick 2004]. Multigrid methods are among the most efficient iterative solution approaches and accelerate convergence by reducing error at multiple spatial resolutions. However, they also have higher fixed overhead costs than methods such as Conjugate Gradient. A GPU implementation of multigrid by Dick et al., [2011b] has demonstrated further speed improvement. Preconditioning can also be used to speed up the iterative solvers. In [Courtecuisse et al. 2010], the authors have demonstrated the asynchronous update of Cholesky factors for preconditioning on a separate thread. The asynchronous update of the factors is similar to our re-factorization scheme. The need for a multi-resolution mesh makes multigrid naturally suited for structured meshes, with hexahedral grids typically being used. Although hexahedral grids do not lend themselves to smooth cutting surfaces, recent work by Zhu et al. [2010] has demonstrated a way to incorporate cutting into a simulation with a multigrid solver.

A final category of iterative solvers is explicit integration methods. Explained in detail in [Bathe 1996], it was originally suggested for use in surgery simulation by Bro-Nielsen [1998] and also implemented in the software suite described in [Joldes et al. 2009]. Explicit integration has been successfully used in real-time simulation with dynamic and non-linear finite element models [Wu et al. 2001], and has been used in simulations involving surgery [Wittek et al. 2010] and cutting [Serby et al. 2001]. Care must be taken in selecting the time step size for explicit integration because it can be numerically unstable if the time steps are too large.

2.3 Hybrid Solution Methods

Some simulations have been implemented using hybrid approaches that use two or more solution methods. Typically, some portion of a model is designated as susceptible to cuts and deformation while the remainder is subject only to deformation. The strategy is to apply a fast pre-computation approach to the portion of a model that cannot be cut and apply a slower method that supports cutting to the remainder. For example, Wu and Heng [2005] [Heng et al. 2004] combine the use of condensation and Conjugate Gradient solvers, while Cotin et al. [2000] combine the use of a linear superposition method with explicit integration applied selectively to the dynamic, cuttable portion of a mesh. Kocak et al. [2009] provided further support for this approach by describing a framework for building a consistent finite element simulation when different regions of the mesh are solved at different update rates.

3. METHODS

The augmented matrix approach presented here is a hybrid solution method that employs both direct and iterative solution algorithms without restricting cutting to a specific part of a model. An $LDL^\top$ factorization computed by a direct solver is used in conjunction with the generalized minimal residual method (GMRES), an iterative algorithm. Applied together, these methods compute fast and accurate solution updates for a finite element model as it undergoes stiffness matrix changes, including topological changes due to cutting.

This section is organized into three parts. First we show how matrix augmentation can be used to express changes to a stiffness matrix. Next we outline the steps required to solve an augmented system of finite element equations. Finally, we detail how the sparsity inherent in the equations can be exploited to maximize the efficiency of the implementation.

3.1 Augmented Finite Element Matrices

In an elastostatic finite element model, an object is represented by a discrete mesh governed by a system of linear equations $Ka = f$, where K is the $n \times n$ global stiffness matrix, a represents nodal displacements, and f represents forces applied to mesh nodes. These are finite element matrices and vectors that are constructed using standard finite element methods [Bathe 1996]. Here n is the number of degrees of freedom in the model; for a 3D solid model n equals three times the number of mesh nodes.

If the i^{th} degree of freedom is involved in a change to the model, the i^{th} row and the i^{th} column of K will be modified to reflect the change in its relationship with the rest of the mesh. Changing any portion of K invalidates a previous factorization, thus necessitating a re-factorization or an update. For a 3D finite element model represented on a mesh with good aspect ratios, stiffness matrix re-factorization can be performed in $O(n^2)$ operations [Lipton et al. 1979]. While this is better than the $O(n^3)$ complexity of matrix inversion, it does not provide the solution speed needed for interactive simulations.

The augmented formulation reflects changes to any limited portion of K while preserving the utility of its pre-computed $LDL^\top$ factors. We rely on an effective column replacement procedure applied to a matrix as follows. Suppose we want to replace the third column of a matrix K^0 in a system with a vector k and compute the solution to the modified system. We can form the following augmented system of equations that, if exact arithmetic is used, will yield the same solution as the modified system after appropriate permutation of the solution vector.

$$\left[\begin{array}{c|c} K^0 & k \\ \hline e_3^\top & 0 \end{array}\right] \begin{bmatrix} a_1 \\ a_2 \\ z_3 \\ a_4 \\ \vdots \\ a_3 \end{bmatrix} = \begin{bmatrix} f_1 \\ f_2 \\ f_3 \\ f_4 \\ \vdots \\ 0 \end{bmatrix}, \tag{1}$$

where $e_3^\top$ is the third row vector of the identity matrix, and z_3 is a placeholder variable at the third component of the solution vector.

Notice that multiplying the a vector by the last row of the augmented matrix constrains z_3 to be 0, and thus the whole third column of K^0 is multiplied by 0, canceling its effect on the system of equations. As the variable a_3 is multiplied by k, this column acts as a replacement for the third column of K^0. This augmentation can be cascaded to replace multiple columns at the same time.

Suppose K, the global stiffness matrix at time $t > t_0$, differs from K^0, the initial stiffness matrix at time t_0, by m columns. We can use the aforementioned effective column replacement procedure on these m columns to form an equivalent, augmented system of equations

$$K^A a^A = f^A, \tag{2}$$

where superscript A suggests that the matrix and vectors are in augmented forms.

All topological mesh changes, including those resulting from cutting or element subdivision, can be represented in a finite element system of equations by replacing or deleting existing stiffness matrix columns and expanding the matrix to accommodate new columns. As described in [Bathe 1996], the global stiffness matrix for a model is assembled by summing the contributions of the stiffness matrices of the individual elements. When a mesh is cut, the affected elements can be removed from the mesh by subtracting their contributions from the global stiffness matrix. Then a set of replacement elements that respect the cut can be added to the global stiffness matrix using the standard assembly procedure. For a large mesh with a localized cut, this results in a small percentage of columns in the global stiffness matrix being changed. These changes can be implemented for a previously factored matrix using the aforementioned matrix augmentation technique.

Similarly, the imposition of Dirichlet boundary conditions that specify the displacements of selected mesh nodes is accomplished through the removal of the associated degrees of freedom from the finite element equations. In the standard formulation this is accomplished by deleting the associated rows and columns from the stiffness matrix. In the augmented matrix formulation, degrees of freedom are removed via steps that resemble the effective column replacement procedure in Eqn. 1. The following example illustrates removal of the third degree of freedom from the augmented system.

$$\left[\begin{array}{c|c} K^0 & e_3 \\ \hline e_3^\top & 0 \end{array}\right]\begin{bmatrix} a_1 \\ a_2 \\ z_3 \\ a_4 \\ \vdots \\ -f_3 \end{bmatrix} = \begin{bmatrix} f_1 \\ f_2 \\ 0 \\ f_4 \\ \vdots \\ 0 \end{bmatrix} - \begin{bmatrix} a_3 K e_3 \\ \\ 0 \end{bmatrix}. \tag{3}$$

As seen from Eqn.1, the last row constrains z_3 to be 0. Performing the multiplication of the third row yields

$$K^0_{31}a_1 + K^0_{32}a_2 + K^0_{33}z_3 + K^0_{34}a_4 + \cdots - f_3 = -K^0_{33}a_3.$$

Substituting $z_3 = 0$ and rearranging the terms would get back the third row of the standard formulation. Similarly, performing the multiplication of the i^{th} row other than the third row yields

$$K^0_{i1}a_1 + K^0_{i2}a_2 + K^0_{i3}z_3 + K^0_{i4}a_4 + \cdots = f_i - K^0_{i3}a_3,$$

which is identical to the i^{th} row of the standard formulation after substitution of $z_3 = 0$ and rearrangements of terms.

Here f_3 is moved from the right-hand-side vector to the solution vector since the force applied to the third degree of freedom becomes unknown after the imposition of Dirichlet boundary condition. Notice the similar structure of Eqns. 1 and 3, demonstrating that both topological changes and imposition of Dirichlet boundary conditions can be accomplished using a unified augmentation procedure. Next we provide the complete algorithm for formulating the augmented system that supports both replacement and expansion affecting multiple matrix columns.

In the ensuing discussion, any matrix or vector without a 0 superscript is assumed to reference the model at some time $t > t_0$. At the beginning of a simulation the augmented system is identical to the standard finite element system at time t_0. For time steps $t > t_0$, K^A retains K^0 as a sub-matrix so that pre-computed factors of K^0 remain useful, and new rows and columns contained in rectangular matrices J and H are appended to account for the updates in K. Mathematically, K^A has the form

$$K^A = \begin{array}{c} \left[\begin{array}{cc|c} K^0 & 0 & \\ 0 & I & J \\ \hline \multicolumn{2}{c|}{H} & 0 \end{array}\right] \begin{array}{l} \left.\vphantom{\begin{array}{c} K^0 \\ 0 \end{array}}\right\} n \\ \left.\vphantom{H}\right\} m \end{array} \\ \underbrace{\hphantom{K^0\;\;0\;\;}}_{n}\underbrace{\hphantom{J\;}}_{m} \end{array}. \tag{4}$$

Here I is the identity matrix with dimension equal to the number of degrees of freedom added to K at times $t > t_0$ corresponding to possible new nodes added to the mesh due to the cut. The columns of I inserted into K^A are effectively replaced by new columns in K. As shown below, J contains a copy of all columns of K that have been added or changed, and H contains rows from the identity matrix. The matrices J and H are defined as

$$J_{*,i} = \begin{cases} K_{*,\mathcal{L}_i} & \text{if } \mathcal{L}_i \notin \mathcal{D} \\ I_{*,\mathcal{L}_i} & \text{if } \mathcal{L}_i \in \mathcal{D} \end{cases}, \text{ and} \tag{5}$$

$$H_{i,*} = I_{\mathcal{L}_i,*}\,. \tag{6}$$

Here $\mathcal{D}$ is the set of degrees of freedom constrained by Dirichlet boundary conditions, and $\mathcal{L}$ is an accessory data structure that maps the indices of columns and rows in J and H to the indices of columns in K^0 to be replaced, i.e. the i^{th} column of J replaces the $\mathcal{L}_i^{\text{th}}$ column of K^0. Hence, the i^{th} column of J contains a copy of the $\mathcal{L}_i^{\text{th}}$ column of K.

Augmented displacement and force vectors must have sizes and degree of freedom orderings consistent with the augmented stiffness matrix. The augmented displacement vector, a^A, can be partitioned into two parts denoted a_1, a vector of length n, and a_2, a vector of length m. Here

$$a^A = \begin{bmatrix} a_1 \\ a_2 \end{bmatrix}, \tag{7}$$

$$(a_1)_i = \begin{cases} a_i & \text{if } i \notin \mathcal{L}, \\ z_i & \text{if } i \in \mathcal{L}. \end{cases} \tag{8}$$

$$(a_2)_i = \begin{cases} a_{\mathcal{L}_i} & \text{if } i \notin \mathcal{D}, \\ -f_{\mathcal{L}_i} & \text{if } i \in \mathcal{D}. \end{cases} \tag{9}$$

As in Eqns. 1 and 3, the z terms are constrained to have a value of zero, the a terms represent unknown nodal displacements, and the f terms represent the unknown nodal forces when a new Dirichlet boundary condition is imposed.

The augmented force vector is also partitioned into two parts: $\hat{f}$ of length n, and a zero vector of length m. Some components of $\hat{f}$ have terms subtracted to account for imposition of new Dirichlet boundary conditions. Here

$$f_i^A = \begin{bmatrix} \hat{f} \\ 0 \end{bmatrix}, \tag{10}$$

$$\hat{f} = \begin{cases} f_i - \sum_{j\in\mathcal{D}} K_{i,j}a_j & i \notin \mathcal{D}, \\ -\sum_{j\in\mathcal{D}} K_{i,j}a_j & i \in \mathcal{D}. \end{cases} \tag{11}$$

The augmentation procedure can be summarized by the following four steps.

(1) Construct the accessory data structures $\mathcal{L}$ and $\mathcal{D}$.

(2) Form matrices J and H using Eqns. 5 and 6. Append J to the right side of the stiffness matrix, K^0, and append H to its bottom as shown in Eqn. 4.

(3) Form the right-hand-side vector f^A using Eqns. 10 and 11.

(4) After computing the solution, copy terms in a^A to the appropriate positions in the nodal displacement and force vectors as indicated by Eqns. 8 and 9, discarding the $z_{\mathcal{L}_i}$ terms.

3.2 Solution Method

Since we assume a conservative material model, the reduced stiffness matrix K is guaranteed to be symmetric positive definite. Thus, it can be factored as $K^0 = L_0\ D_0\ L_0^\top$, where L_0 is a lower triangular matrix and D_0 is a diagonal matrix. If new degrees of freedom are added to the model in subsequent time steps, the factors can be padded as follows.

$$\underbrace{\begin{bmatrix} K^0 & 0 \\ 0 & I \end{bmatrix}}_{R} = \underbrace{\begin{bmatrix} L_0 & 0 \\ 0 & I \end{bmatrix}}_{L} \underbrace{\begin{bmatrix} D_0 & 0 \\ 0 & I \end{bmatrix}}_{D} \underbrace{\begin{bmatrix} L_0^\top & 0 \\ 0 & I \end{bmatrix}}_{L^\top} \tag{12}$$

where I is the identity matrix with dimension equal to the number of columns added to K, as in Eqn. 4. Using the matrix names shown above, the equation can be stated more compactly as $R = LDL^\top$. Note particularly that R refers to the global stiffness matrix from time t_0 padded so that its dimension matches that of K in the current time step.

Substituting the definitions provided in Eqns. 4, 7, 10, and 12 into the augmented system of equations given in Eqn. 2 gives

$$\begin{bmatrix} R & J \\ H & 0 \end{bmatrix} \begin{bmatrix} a_1 \\ a_2 \end{bmatrix} = \begin{bmatrix} \hat{f} \\ 0 \end{bmatrix}. \tag{13}$$

Performing the multiplication in Eqn. 13 yields the following two equations.

$$R\,a_1 + J\,a_2 = \hat{f}. \tag{14}$$

$$H\,a_1 = 0. \tag{15}$$

Eqn. 14 can be rewritten as

$$a_1 = R^{-1}\big(\hat{f} - J\,a_2\big). \tag{16}$$

Substituting Eqn. 16 into Eqn. 15 yields

$$\big(HR^{-1}J\big)\,a_2 = HR^{-1}\hat{f} \tag{17}$$

The solution of Eqn. 13 can then be broken into three steps.

(1) *Calculate the right hand side of Eqn. 17.*
Each occurrence of the multiplication $R^{-1}\,x$, for any vector x, can be efficiently calculated using the pre-computed $LDL^\top$ factors of R via triangular matrix solves with forward and back substitution. We use this observation to first calculate the vector y, where $y = R^{-1}\hat{f}$, and then calculate the product $H\,y$ to arrive at the vector on the right hand side of Eqn. 17.

(2) *Solve Eqn. 17 to find a_2 using an iterative solver.*
Since the right hand side of Eqn. 17 is known from step 1, an iterative solver can be used to successively improve estimates of a_2 if the multiplication $(HR^{-1}J)\,a_2$ can be performed. J and H have known values, and by making use of the $LDL^\top$ factors of R again, multiplication with R^{-1} can be accomplished. As in step 1, performing this multiplication requires triangular matrix solves with forward and back substitution. We use GMRES, a Krylov space iterative solver that requires only one or two matrix-vector multiplications per iteration. This choice minimizes the number of triangular solves needed.

(3) *Substitute a_2 into Eqn. 16, then solve for a_1.*
This step requires the use of the $LDL^\top$ factors a final time to perform the multiplication of R^{-1} with the known vector $\big(\hat{f} - J\,a_2\big)$.

3.3 Accelerated Implementation Using Sparsity

3.3.1 *Exploiting Sparsity in the Solution Steps.* A careful examination of the sparsity of the matrices and vectors in Eqns. 17 and 16 allows us to maximize the efficiency of our implementation. The sparsity analysis is expressed using concepts from graph theory that are outlined in the Appendix. Each of the three solution steps outlined for Eqns. 16 and 17 in Section 3.2 involves computation with sparse vectors and matrices. We carefully exploit this sparsity to avoid unnecessary computation.

Sparsity of Solution Step 1:
The right hand side of Eqn. 17 is evaluated by computing

$$HR^{-1}f = H\,\underbrace{L^{-\top}D^{-1}\left(L^{-1}f\right)}_{y}. \tag{18}$$

By applying Thm. 1 given in the Appendix, we find that $\mathrm{struct}(L^{-1}f) \subseteq \mathrm{closure}_L(f)$. This result says that the nonzero components in the vector in the left-hand-side are given by components that can reach the nonzero components in the vector f by an edge in a directed graph representation of the matrix L. Details are in the Appendix. Hence only the submatrix of L corresponding to $\mathrm{closure}_L(f)$ is needed to evaluate the term $L^{-1}f$. We observe that the vector f is typically sparse because external forces are only applied to a small fraction of the nodes while a mesh is being cut or deformed.

Consider that after we have computed the vector y in Eqn. 18 it is projected through multiplication by the sparse matrix H. H is composed of a few rows from an identity matrix, and it has many more columns than rows. Only m columns of H contain nonzero components and consequently all but m components of y are multiplied by 0 and do not contribute to the value of the right hand side vector. Let the components of y necessary for the calculation be denoted $\hat{y}$, such that $H\hat{y} = Hy$. Then

$$\hat{y}_i = \begin{cases} y_i & \text{if } H_{(*,i)} \neq 0, \\ 0 & \text{otherwise.} \end{cases} \tag{19}$$

By applying Thm. 2 from the Appendix, we find that only the submatrix of $L^\top$ corresponding to $\mathrm{closure}_L(\hat{y})$ is needed to complete the evaluation of the right hand side of Eqn. 17.

Sparsity of Solution Step 2:
During each GMRES iteration in solution step 2, the solution estimate a_2 is projected by a sparse matrix J to a larger space.

$$\big(HR^{-1}J\big)\,a_2 = H\,\underbrace{L^{-\top}D^{-1}L^{-1}\left(Ja_2\right)}_{w}. \tag{20}$$

Because the product vector Ja_2 is sparse, only the submatrix of L corresponding to $\mathrm{closure}_L(Ja_2)$ is useful. As in step 1, the vector w is projected through multiplication by H. Hence, during the backward substitution only a submatrix of $L^\top$ corresponding to $\mathrm{closure}_L(w)$ is needed for the computation.

Sparsity of Solution Step 3:
Since in Step 3 both f and Ja_2 are sparse, the difference vector $f - Ja_2$ is also sparse. Hence the forward substitution can be sped up by considering only those needed rows of L. However, since the solution vector α_1 is not projected by a sparse matrix, the whole matrix $L^\top$ is needed in the backward substitution.

We note that in both Steps 1 and 3 the triangular solves are only done once, so we modify these routines to accept two additional inputs that indicate the sparsity of the right hand side vector and the indices of needed components in the solution vector. However, the

	Computation	Complexity
Initialization: $t = t_0$		
1	Compute $LDL^\top$ factorization of K^{A_0}	$O(n^2)$ for 3D meshes; $O(n^{3/2})$ for 2D meshes
Real-time update steps: $t > t_0$		
1	Update K	$O(m)$
2	Compute J and H	$O(m)$
3	Solution Step 1	$O(\lvert\, \mathrm{closure}_L(f)\,\rvert + \lvert\, \mathrm{closure}_L(\hat{y})\,\rvert) \le O(\lvert L\rvert)$
4	Solution Step 2	$O(\lvert\, \mathrm{closure}_L(Ja_2)\,\rvert + \lvert\, \mathrm{closure}_L(\hat{y})\,\rvert) \cdot n_{iter} \le O(\lvert L\rvert \cdot n_{iter})$
5	Solution Step 3	$O(\lvert L\rvert)$

Table I. : A summary of the calculation steps required by the augmented method is shown, along with a complexity bound for each step. Here n is the order of the initial stiffness matrix, m is the number of columns changed by cutting, and $|L|$ in solution steps 1, 2 & 3 is the number of non-zeros in L, which is bounded by $O(n^{4/3})$ for 3D meshes and $O(n \log n)$ for 2D meshes. The complexity upper bound for an entire update iteration is $O(|L| \cdot n_{iter})$, where n_{iter} is the number of GMRES iterations needed for convergence.

situation is different for step 2, where GMRES executes multiple iterations before converging. In this case, to reduce the overhead of indirect indexing we explicitly form the needed submatrices by copying the needed rows and columns from L and $L^\top$.

3.4 Complexity Analysis

Key parts of the complexity analysis hinge on the sparsity of the stiffness matrix, the complexity of the $LDL^\top$ factorization, and the sparsity of the factors. The number of non-zeros in each column of the global stiffness matrix is dependent on the connectivity between nodes. Since in a well-formed mesh the number of edges incident on a single node is limited by geometric considerations, the number of non-zeros per column can be bounded by a constant that is independent of the total number of degrees of freedom in the model. Due to this assumption and since sparse matrix data structures are used in this work, the complexity of all the steps in the augmented algorithm that update or otherwise operate on stiffness matrix columns is dependent only on the number of columns affected, not the number of rows in the matrix.

The derivation of complexity bounds for the $LDL^\top$ factorization can be found in [Lipton et al. 1979]. Their work shows that using efficient sparse matrix algorithms, an $LDL^\top$ factorization of an $n \times n$ stiffness matrix for a 3D finite element model can be accomplished with $O(n^2)$ operations; the resulting lower triangular matrix L will contain $O(n^{4/3})$ non-zeros if the mesh elements have good aspect ratios. Therefore, without imposing any restrictions on the force vector, we can say that the triangular solves needed in steps 1 and 3 of the solution algorithm described in Section 3.2 can be completed in $O(n^{4/3})$ operations.

Considering the sparsity analysis in the previous section raises the question of whether sparsity could provide a basis for a tighter complexity bound. In solution step 1, the complexity depends on $|\,\mathrm{closure}_L(f)\,|$ and $|\,\mathrm{closure}_L(\hat{y})\,|$. Theorem 3 from the Appendix informs us that the sizes of the closures depend on the length of the path from the root of the elimination tree to the nodes in $\mathrm{struct}(f)$ and $\mathrm{struct}(\hat{y})$. If those nodes are close to the root, the sizes would be small constants, independent of n. On the other hand, if they are leaves of the elimination tree, the sizes would be close to n, and the cost of the triangular solve step would be linear in the number of nonzeros in L, $O(n^{4/3})$. In general, the cost lies in between these two extremes, and the upper bound of $O(n^{4/3})$ is not tight.

The complexity for each step in the algorithm, including the pre-computation phase and the real-time update loop, is detailed in Table I. Summing the complexity of each of the real-time update steps for a 3D model and simplifying the expression to retain only the dominant terms results in a complexity bound for an update iteration of $O(n^{4/3} \cdot n_{iter})$, where n_{iter} is the number of GMRES iterations needed for convergence. Note that n_{iter} is influenced by m, the number of columns updated, rather than n, the dimension of the stiffness matrix.

3.5 Preconditioning

The GMRES iteration in step 2 can be preconditioned to reduce the number of iterations. One possible preconditioner is a matrix M that approximates $HR^{-1}J$ in Eqn. 17. However, there are two drawbacks of this approach: neither forming the matrix $HR^{-1}J$ nor minimizing $\|M(HR^{-1}J)-I\|$ is computationally cheap. Also, M has to be recomputed whenever there is a change to the mesh. Another possible preconditioner is a matrix product HSJ such that S approximates R^{-1}. In this case, S only needs to be computed once and can be reused in later time steps, even after changes to the mesh. In this paper, we use two approximations of S: the inverse of D in the pre-computed $LDL^\top$ factors of R (for all meshes), and a tridiagonal sparse approximate inverse (SPAI) [Benson and Federickson 1982] of the matrix R (for Stanford Bunny, brain and eye meshes).

3.6 Re-factorization

The augmented matrix approach produces a solution for a finite element model with a time-varying stiffness matrix more quickly than a full re-factorization would allow, so long as m, the number of modified columns, is sufficiently small. As changes to a stiffness matrix accumulate across a growing number of columns, the augmented method begins to slow down because the size of the a_2 vector also increases. To maintain fast solution speeds for an interactive simulation, we prevent m from growing indefinitely by periodically re-computing a full $LDL^\top$ factorization of K in a process that runs concurrently with the simulation loop. Fig. 1 shows the changes in the equations before and after re-factorization. Let m' denote the number of columns modified due to cutting after the re-factorization was initiated. When freshly computed factors are used to replace the original factors, the size $m + m'$ is reduced to

m'. The rate at which matrix changes accumulate will vary widely and depend both on the nature of a simulation and how quickly and aggressively a user manipulates a model. Even considering a single user and a single simulation, the growth rate of m will vary unevenly across time as an interactive task progresses through moments of cutting, grasping, and pulling. Since the speed of our solution method is dependent on $m+m'$, the simulation update rate it provides is affected by the speed of mesh cutting and other manipulations. The best way to address this issue will be depend on the application, but in some contexts it is reasonable to limit the rate at which cutting can occur in order to maintain an desired update rate. Variability in the update rate arising from the re-factorization process can be smoothed by buffering the computed solutions.

To provide some context for how re-factorization will impact simulation speed, the results in Figs. 5, 7, 10a, 12 and 13 indicate the simulation step at which the cumulative time for mesh updates equals the time for matrix factorization, assuming one newly cut node per update and beginning with an empty list of mesh modifications. In practice, the list of recent mesh modifications will be

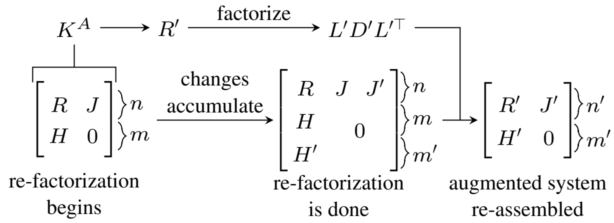

Fig. 1: Re-factorization process

non-empty when a re-factorization step completes, there will be update steps that involve changes to multiple nodes, and many update steps will not involve any topological mesh changes. Depending on these factors, actual simulation updates rates could be faster or slower when re-factorization concludes than the times shown in the graphs. It is also feasible to run multiple re-factorization processes concurrently, so that mesh changes get incorporated into the factors

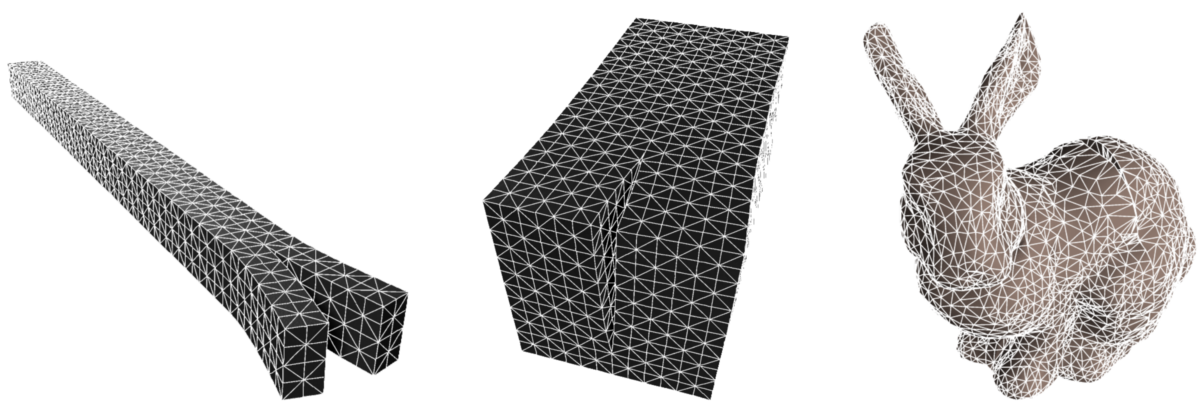

(a) (b) (c)

Fig. 2: Test meshes are shown after cuts described in the experiments in Section 4.2.

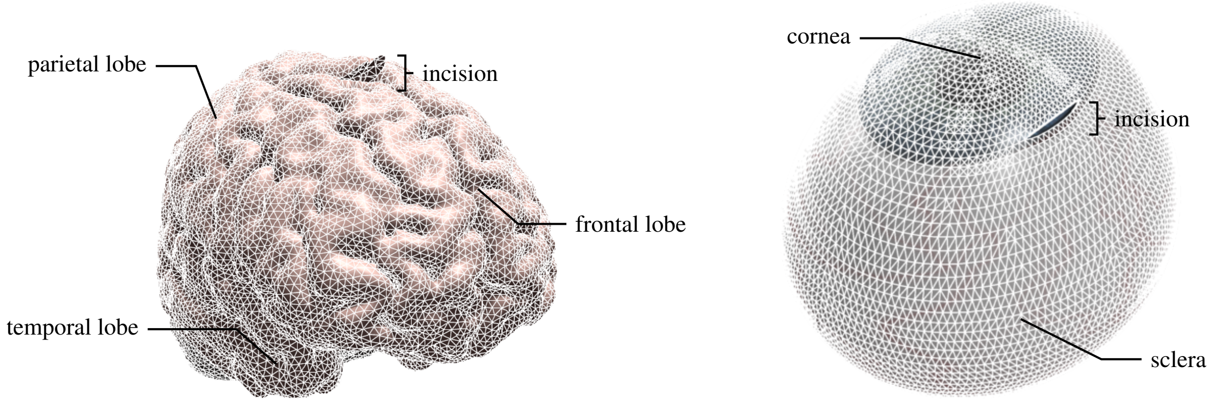

(a) (b)

Fig. 3: Renderings of brain and eye models are shown with incisions used in the experiments reported in Section 4.2. (a) The incision on the brain model shown is on the superior portion of the right frontal lobe. (b) The incision on the eye model shown is along the corneal limbus, to correct for astigmatism.

as quickly as possible and the size of m is kept to a minimum. If multiple processors are available, this is one way to maximize the update rate since it is not necessary for one factorization process to complete before another one begins.

4. RESULTS

The augmented matrix solution method was evaluated through finite element deformation and cutting experiments with five model types. This section provides relevant implementation details and presents experimental data, including comparisons with both non-preconditioned and Jacobi-preconditioned Conjugate Gradient (CG) solvers. ILU0 and ILUT preconditioners for CG were tested, but the reduction in number of iterations did not compensate for the increased computation complexity per iteration.

4.1 Implementation

All experiments were conducted on a desktop computer with four 8-core Intel Xeon E5-2670 processors running at 2.6GHz with 20 GB cache and 256 GB RAM. All data represent an average timing from 20 runs.

The precomputed $LDL^\top$ factorizations of the stiffness matrices were computed using OBLIO, a sparse direct solver library [Dobrian and Pothen 2006]. Both the GMRES iterative solver used in solution step 2 and the CG solver used for comparison purposes were from the Intel Math Kernel Library (MKL). The remainder of the code was written by the authors.

All matrices were stored in sparse matrix format to reduce both the storage space and access time. Since the closure of a set of indices in the graph of a triangular matrix can be found effectively column by column, and OBLIO uses supernodes in matrix factorization, all matrices were stored in compressed sparse column (CSC) format for efficient column access.

4.2 Model Meshes

Five types of solid tetrahedral meshes were used to evaluate the augmented matrix solution method in comparison to a traditional CG method. Meshes are shown in Figs. 2 and 3.

(1) *Elongated Beam:* A group of five elongated rectangular solids with varying lengths were generated. Nodes were placed at regularly spaced grid points on a $5 \times 5 \times h$ grid, where h ranged from 4 to 1024. The largest beam mesh has $25,600$ nodes and $81,840$ elements. Each block mesh was anchored at one end of the solid. All elements had good aspect ratios and were arranged in a regular pattern. However models with greater degrees of elongation produced more poorly conditioned systems of equations, as fixation at only one end meant that longer structures were less stable. Thus experiments with this group of meshes illuminates the way solver performance varies with stiffness matrix conditioning. The estimated condition numbers of the beam mesh stiffness matrices range from 1.14×10^3 to 3.29×10^{12}.

(2) *Brick:* A group of five rectangular brick solids with varying mesh resolutions were generated. Each of the models had the same compact physical dimension of $1 \times 1 \times 2$. An initial good-quality mesh was uniformly subdivided to produce meshes of increasingly fine resolution. These meshes allowed us to examine solver performance relative to node count for fixed model geometry. Similar to the beam meshes, zero-displacement boundary conditions were applied to one face of the block. The largest brick mesh has $18,081$ nodes and $80,000$ elements. The estimated condition numbers of the brick mesh stiffness matrices range from 2.19×10^3 to 1.18×10^5.

(3) *Stanford bunny:* A $20,133$ node, $62,698$ element mesh of the Stanford bunny [Turk and Levoy 1994] is used to demonstrate solver performance on an irregular mesh. Zero-displacement boundary conditions are applied to nodes on the bottom of the bunny's feet. The bunny mesh stiffness matrix has an estimated condition number of 6.17×10^7.

(4) *Eye:* Incisions into a human eye model [Crouch and Cherry 2007] were used to demonstrate applicability to surgery simulation. Clear cornea cataract incisions were made into two models with resolutions containing $4,444$ nodes and $14,841$ elements, and $16,176$ nodes and $52,772$ elements. Zero displacement boundary conditions were applied to the posterior portion of the globe. The eye mesh stiffness matrices have estimated condition numbers of 2.66×10^6 and 1.62×10^7 respectively.

Relaxing limbal incisions used to treat severe astigmatism were also simulated using the eye models. Simulation of the relaxing limbal incision procedure is of particular interest because the deformation induced by the incisions is not incidental to the procedure but rather is the motivating reason for performing the procedure. Astigmatism causes blurred vision due to an aspherical corneal surface, meaning the corneal curvature is higher along some cross-sections than others. This variation in curvature can be reduced for patients through limbal incisions that are carefully placed around the periphery of the cornea to create a flattening effect along the meridian of highest curvature. Although guidelines exist for selecting appropriate placement, depth, and length for these incisions, such guidelines make a number of assumptions about a patient's eye anatomy and cannot fully account for individual variations in corneal topography and thickness. Thus, simulations of this procedure might be useful both for individualizing treatment plans and as a teaching tool in medical education. While the tissue motion that is induced by relaxing limbal incisions is measured in millimeters, the resulting change in the optics of the cornea can be very significant, correcting up to 3 diopters of astigmatism. Since the cornea is responsible for two-thirds of the focusing power of the eye, small changes in corneal curvature can have a large impact on visual acuity. A linear elastic material model is appropriate for this application because the deformations are small in absolute terms. However, large, medically important changes in patients' refractive error result from these small deformations.

(5) *Brain:* Two resolutions of a human brain model (contributed by INRIA to the AIM@SHAPE Shape Repository) were used to demonstrate applicability to surgery simulation on an organ of complicated structure. The models contained $23,734$ nodes and $81,746$ elements, and $50,737$ nodes and $167,366$ elements. Zero displacement boundary conditions were applied to the interior portion of the brain. The small brain mesh stiffness matrix has estimated condition number of 4.64×10^7. The condition estimation failed for the large brain mesh due to insufficient memory.

On average, the nodes in the brick meshes have a higher degree of connectivity than those in the elongated beam meshes. This is due to a greater proportion of surface nodes in the beam models versus interior nodes in the brick models. The increased connectivity leads to a higher percentage of non-zeros in the stiffness matrix factors and larger sizes for the closures referenced in Table 1.

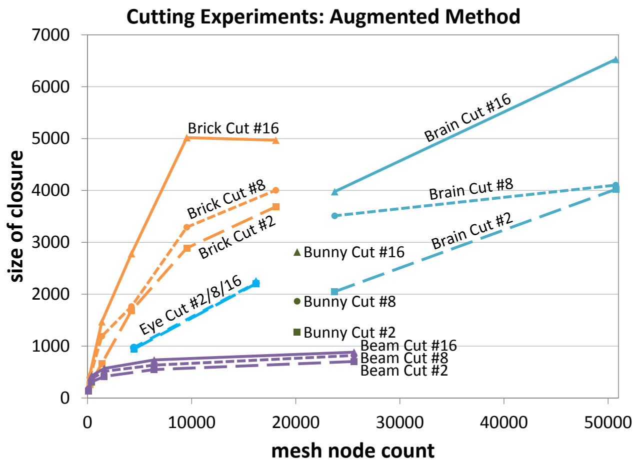

Fig. 4: $|\,\mathrm{closure}_L(Ja2)\,|$ vs. node count, shown for cutting steps 2, 8, and 16.

These differences have a significant impact on the relative performance of the solution methods. Fig. 4 compares $|\,\mathrm{closure}_L(Ja2)\,|$ for the different test meshes during the cutting experiments. The set $\mathrm{closure}_L(Ja2)$ is the largest of the closures referenced in the complexity analysis in Table I, and is a measure of the size of the triangular system to be solved. As expected, brick meshes have larger closures than the other two meshes.

4.3 Experiments

Performance was examined through two types of experiments: deformation of intact meshes, and deformation of meshes undergoing cutting.

4.3.1 *Deformation of Intact Meshes.* In this group of experiments, we applied an increasing number of non-zero essential boundary conditions to mesh nodes to create deformation. Fig. 5 shows how solution time varied with the number of constrained nodes for instances of the beam and brick meshes. It is interesting to note the dramatically different results for the beam meshes versus the brick meshes in these experiments. As shown in Fig. 5(a), the augmented method maintained a high update rate for the beam meshes throughout, and vastly outperformed the CG method. The beam deformation experiments ran so fast with the augmented method that the experiments concluded before there was time to compute a re-factorization. In the example shown in the figure, the update cycles ran at rates between 137–263 Hz.

For brick meshes, the augmented method outperformed CG as constraints were applied to the first one to two dozen nodes, but performance dropped as the number of constrained nodes increased, eventually resulting in similar update rates between the augmented method and CG. However, since the brick mesh experiments ran more slowly overall, re-factorization played a meaningful role in the augmented solution process. In the results shown in Fig. 5(b), a re-factorization process running concurrently with the solution loop completed after approximately 16 deformation steps. Thus we see that the augmented method outperformed CG by a modest margin in the brick deformation experiment.

Fig. 6 is a log-log plot that shows how solution times varied for different sizes of beam and brick meshes. These graphs show that the augmented method ran significantly faster than CG for the beam meshes except for the very smallest instance that had only 100 nodes. Most strikingly, on the largest beam mesh, which had 25,600 nodes, the augmented method provided updates at a rate of 113 Hz, while CG ran at 3×10^{-5} Hz. For the brick meshes, the augmented method ran faster than CG, although the margin was smaller.

4.3.2 *Deformation of Meshes Undergoing Cutting.* In this group of experiments we made an advancing planar cut into the volume of each mesh. As a cut progressed, a duplicate of each node along the cut path was added to the mesh, and connectivity was modified so that elements on opposite sides of the cut became separated. These changes required expanding the stiffness matrix and modifying existing entries in the stiffness matrix at dozens of locations each time a node was duplicated. Opposing force vectors were applied to selected surface nodes to pull the cut faces apart. Fig. 2 shows the three test meshes at the initial stages of cutting.

The differences between the results for the beam and brick meshes are even more pronounced for the cutting experiment than for the deformation experiment. Fig. 7(a) shows that the augmented method outperformed CG in the beam cutting experiments, providing updates in the range 49–145 Hz in the time period before the re-factorization completed. CG provided updates in the range 0.26–172 Hz for the same cutting steps, but failed to converge to any solution for seven of those steps. However, CG provided consistently better performance for the brick mesh cutting experiment, as shown in Fig. 7(b). The zig-zag appearance of the CG results was caused by the connectivity pattern of nodes in the tetrahedral brick mesh. Periodically, nodes with a higher degree of connectivity were cut. These cutting steps required a larger number of changes to the stiffness matrix and resulted in periodically slower CG solution times. The connectivity pattern is illustrated in Fig. 8.

Fig. 9 shows that the beam vs. brick performance trend held over a variety of mesh sizes. The augmented method provided the fastest updates when cutting a beam mesh, maintaining an update rate over 50 Hz even with a relatively large cut in a 25,600 node mesh. Particularly for the larger beam meshes, CG was often unable to provide any solution. However, CG reliably provided the fastest updates when cutting a brick mesh.

Results from the bunny mesh cutting experiment are shown in Fig. 10. Here we find that the non-preconditioned augmented

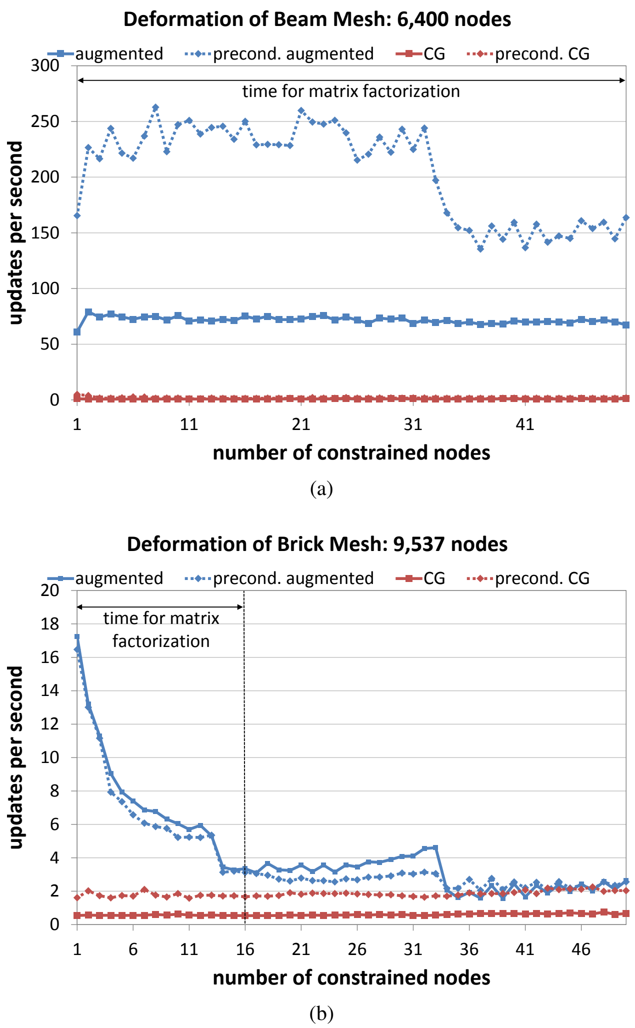

Fig. 5: Deformation update rates are shown for both the augmented and CG methods as constraints are progressively added to an increasing number of nodes in (a) beam and (b) brick meshes.

method performed best, with a minimum update rate of 14 Hz during the period before re-factorization completes. As seen in some of the previous experiments, the update rate provided by the augmented method diminishes as the size of the cut and complexity of the attendant remeshing grows. However, the augmented method is still faster than the 0.3–6.8 Hz update rate provided by preconditioned CG in this experiment. Fig. 10(b) shows that the bulk of the computation time is spent in the GMRES iteration of Step 2 in the bunny mesh cutting experiment. The dominance of the GMRES iterations in the distribution of computing time is also a feature of the experiments with beam and brick meshes. However, Fig. 11(a) demonstrates that the number of GMRES iterations needed for convergence does not grow with model size.

Results from the eye mesh cutting experiments are shown in Fig. 12, and those from the brain mesh cutting experiments are shown in Fig. 13. Here we show that augmented method outperformed the CG method with and without preconditioning. However, the update rate for the brain meshes remains lower than desired for interactive simulation, and further reduction of the solution times for large, dense meshes is a priority for future work.

The experimental results also indicate that the augmented solution method does not lead to problems with solution accuracy. Fig. 11(b) shows that the relative error of the computed solutions remains flat as a brick mesh is cut and increases only gradually as the less stable beam mesh is cut.

5. CONCLUSIONS AND FUTURE WORK

There are two primary reasons for the disparity between the beam mesh and brick mesh results. First, the beam meshes have a higher percentage of surface nodes, resulting in sparser matrix factors and smaller closure sizes, as shown in Fig. 4. Smaller closures result in faster execution of the augmented solution steps, particularly the GMRES iterations in Step 2. Thus we see that the structure of a mesh is an important factor in determining whether the augmented method will be a particularly efficient solution method for a given problem. In general, the augmented method is particularly attractive for meshes that have greater amounts of surface area relative to their volume.

The second reason for the wide disparity in results is that the brick meshes had particularly well-conditioned stiffness matrices while the beam meshes had more poorly conditioned stiffness matrices. Iterative methods can converge very slowly or fail to converge at all when systems are not sufficiently well-conditioned. In contrast, the direct solution approach provided by the augmented factors is more robust in poorly conditioned scenarios. We conclude that the augmented method is particularly appropriate when a problem would benefit from the robustness of a direct solution approach but also needs the flexibility to update the system due to cutting or other changes.

In summary, we have demonstrated the feasibility of using augmented matrices to provide fast updates for finite element models undergoing cutting and deformation. The augmented method has been experimentally shown to offer advantages both in speed and reliability for certain classes of problems. We plan to explore the applicability of this method to a wider range of problems in future work. One particular application to investigate is surgery simulation, where there is evidence that viscoelastic and hyperelastic material models are often appropriate for soft tissues modeling [Fung 1993] [Lapeer et al. 2010] [Marchesseau et al. 2010]. Non-linear material models can require stiffness matrix updates at each time step, even without cutting. However, in the case of tool-tissue interaction, acceptable non-linear accuracy might possibly be achieved by only updating the stiffness of a subset of the most deformed elements or those closest to the contact area. This raises the interesting possibility of using the augmented matrix method for fast updates of non-linear materials.

Another direction for future investigation is inspired by the variety of recent publications that have reported acceleration of solution methods via GPU implementations [Dick et al. 2011b] [Courtecuisse et al. 2010] [Joldes et al. 2010] [nVidia 2013]. Our augmented matrix solution method could likely be similarly accelerated if the triangular solves and/or GMRES algorithm were implemented in a way that makes efficient use of GPU processing.

APPENDIX

Graph theory concepts relied upon in the discussions of sparsity and complexity are outlined here. Included are the definitions and Theorems referenced in Section 3.3. Note that in this discussion the matrix A is nonsymmetric. We apply these results to the lower and upper triangular factors of the stiffness matrix K, although the results here are more general.

DEFINITION 1. *An $n \times n$ sparse matrix A can be represented by a directed graph $G(A)$ whose vertices are the integers $1, \dots, n$ and whose edges are*

$$\{(i, j) : i \neq j, \textit{ and } A_{ij} \neq 0\}.$$

This set of indices is called the structure of A.

DEFINITION 2. *The transitive reduction of a directed graph $G(L)$ is the graph obtained by removing edges (i, j) whenever there is a directed path (that does not use the edge (i, j)) joining vertices i and j. An elimination tree of a Cholesky factor L is the transitive reduction of the directed graph $G(L)$ (in this case it is a tree rather than a directed acyclic graph). [Liu 1990]*

DEFINITION 3. *The structure of a vector x with n components is*

$$\mathrm{struct}(x) := \{i : x_i \neq 0\},$$

which can be interpreted as a set of vertices, $\mathbb{W}$, of the directed graph of $G(A)$ such that $i \in \mathbb{W}$ if and only if $x_i \neq 0$ when solving $Ax = b$ or $Ay = x$. In this paper, for a vector x, $\mathrm{closure}_A(x)$ refers to $\mathrm{closure}_A(\mathrm{struct}(x))$.

DEFINITION 4. *Given a directed graph $G(A)$ and a subset of its vertices denoted by $\mathbb{W}$, we say $\mathbb{W}$ is closed with respect to A if there is no edge of $G(A)$ that joins a vertex not in $\mathbb{W}$ to a vertex in $\mathbb{W}$; that is, $v_j \in \mathbb{W}$ and $A_{ij} \neq 0$ implies $v_i \in \mathbb{W}$. The closure of $\mathbb{W}$ with respect to A is the smallest closed set containing $\mathbb{W}$,*

$$\mathrm{closure}_A(\mathbb{W}) := \bigcap\{\mathbb{U} : \mathbb{W} \subseteq \mathbb{U}, \textit{ and } \mathbb{U} \textit{ is closed}\},$$

which is the set of vertices of $G(A)$ from which there are directed paths in $G(A)$ to vertices in $\mathbb{W}$.

THEOREM 1. *Let the structures of A and b be given. Whatever the values of the nonzeros in A and b, if A is nonsingular then*

$$\mathrm{struct}(A^{-1}b) \subseteq \mathrm{closure}_A(b)\,.$$

The proof of Theorem 1 can be found in [Gilbert 1994].

THEOREM 2. *Suppose we need only some of the components of the solution vector x of the system $Ax = b$. Denote the needed components by $\hat{x}$. If A is nonsingular, then the set of components in b needed is $\mathrm{closure}_{A^\top}(\hat{x})$.*

PROOF. Let values be given for which A is nonsingular. Renumber the vertices of $G(A^\top)$ so that $\mathrm{closure}_{A^\top}(\hat{x}) = \{1, 2, \dots, k\}$ for some $k \leq n$. Then $Ax = b$ can be partitioned as

$$\begin{pmatrix} B & D \\ C & E \end{pmatrix} \begin{pmatrix} y \\ z \end{pmatrix} = \begin{pmatrix} d \\ e \end{pmatrix},$$

where B is $k \times k$. By the definition of $\mathrm{closure}_{A^\top}(\hat{x})$, there is no edge (i, j) with $i \in \mathrm{closure}_{A^\top}(\hat{x})$ and $j \notin \mathrm{closure}_{A^\top}(\hat{x})$. Therefore $D = 0$. Then $By = d$. Since A is nonsingular, B is also nonsingular. Thus $\hat{x}$ can be computed by solving only $By = d$, which implies only $\mathrm{closure}_{A^\top}(\hat{x})$ is needed to compute the components in $\hat{x}$. $\square$

THEOREM 3. *Let $A = LL^\top$ be a Cholesky factorization and $\mathbb{W}$ be a subset of vertices in $G(L)$. If r is the root of the elimination tree T of L, then*

$$\mathrm{closure}_L(\mathbb{W}) = \bigcup_{v \in \mathbb{W}} \{r \overset{T}{\Rightarrow} v\},$$

where $r \overset{T}{\Rightarrow} v$ is the path from r to v in T, including all intermediate vertices along the path.

PROOF. (i) $\bigcup_{v \in \mathbb{W}} \{r \overset{T}{\Rightarrow} v\} \subseteq \mathrm{closure}_L(\mathbb{W})$:

For any edge between a node v and its parent u in T, there is an edge (u, v) in $G(L)$. By definition if $v \in \mathrm{closure}_L(\mathbb{W})$, then $u \in \mathrm{closure}_L(\mathbb{W})$. Since $\mathbb{W} \in \mathrm{closure}_L(\mathbb{W})$, all ancestors of W must be in $\mathrm{closure}_L(\mathbb{W})$.

(ii) $\mathrm{closure}_L(\mathbb{W}) \subseteq \bigcup_{v \in \mathbb{W}} \{r \overset{T}{\Rightarrow} v\}$:

If a node $u \notin \bigcup_{v \in \mathbb{W}} \{r \overset{T}{\Rightarrow} v\}$, there must be a path from a node

$w \in \bigcup_{v \in \mathbb{W}} \{r \overset{T}{\Rightarrow} v\}$ to u. Hence there is also a directed path from w to u in $G(L)$. Since L is lower triangular, there is no cycle in $G(L)$. Hence there is no directed path from u to w and $u \notin \text{closure}_L(\mathbb{W})$.

□

ACKNOWLEDGMENTS

We are grateful to the owners of the models used in the experiments. The Stanford bunny model is provided courtesy of the Stanford Computer Graphics Laboratory by the Stanford 3D Scanning Repository. The human eye model was created by one of us (JRC). The human brain model is provided courtesy of INRIA by the AIM@SHAPE Shape Repository. We thank the reviewers for their careful reading and helpful suggestions.

REFERENCES

ANDREAUS, U., GIORGIO, I., AND MADEO, A. 2014. Modeling of the interaction between bone tissue and resorbable biomaterial as linear elastic materials with voids. *Zeitschrift für angewandte Mathematik und Physik 66,* 1, 209–237.

BATHE, K. 1996. *Finite Element Procedures*. Prentice-Hall, New Jersey.

BENSON, M. W. AND FEDERICKSON, P. O. 1982. Iterative solution of large sparse linear systems arising in certain multidimensional approximation problems. *Utilitas Mathematica 22*, 127–140.

BERKLEY, J., TURKIYYAH, G., BERG, D., GANTER, M., AND WEGHORST, S. 2004. Real-time finite element modeling for surgery simulation: An application to virtual suturing. *IEEE Trans. on Visualization and Computer Graphics 10,* 3 (May.-Jun.), 314–325.

BERKLEY, J., WEGHORST, S., GLADSTONE, H., RAUGI, G., BERG, D., AND GANTER, M. 1999. Banded matrix approach to finite element modeling for soft tissue simulation. *Virtual Reality: Research, Development & Applications 4*, 203–212.

BRO-NIELSEN, M. 1998. Finite element modeling in surgery simulation. *Proc. of the IEEE 86,* 3 (Mar.), 490–503.

BRO-NIELSEN, M. AND COTIN, S. 1996. Real-time volumetric deformable models for surgery simulation using finite elements and condensation. *Computer Graphics Forum 15,* 3, 57–66.

CHEN, Y., DAVIS, T. A., HAGER, W. W., AND RAJAMANICKAM, S. 2008. Algorithm 887: CHOLMOD, supernodal sparse Cholesky factorization and update/downdate. *ACM Transactions on Mathematical Software 35*, 22:1–22:14.

CHENTANEZ, N., ALTEROVITZ, R., RITCHIE, D., CHO, L., HAUSER, K. K., GOLDBERG, K., SHEWCHUK, J. R., AND O'BRIEN, J. F. 2009. Interactive simulation of surgical needle insertion and steering. *ACM Trans. on Graphics 28,* 3 (July), 88:1–88:10.

COTIN, S., DELINGETTE, H., AND AYACHE, N. 1999. Real-time elastic deformations of soft tissues for surgery simulation. *IEEE Trans. on Visualization and Computer Graphics 5,* 1, 62–73.

COTIN, S., DELINGETTE, H., AND AYACHE, N. 2000. A hybrid elastic model for real-time cutting, deformations, and force feedback for surgery training and simulation. *The Visual Computer 16,* 7, 437–452.

COURTECUISSE, H., ALLARD, J., DURIEZ, C., AND COTIN, S. 2010. Asynchronous preconditioners for efficient solving of non-linear deformations. In *Proc. of Virtual Reality Interaction and Physical Simulation*. 59–68.

COURTECUISSE, H., JUNG, H., ALLARD, J., DURIEZ, C., LEE, D. Y., AND COTIN, S. 2010. GPU-based real-time soft tissue deformation with cutting and haptic feedback. *Progress in Biophysics & Molecular Biology 103,* 23, 159–168.

COVER, S., EZQUERRA, N., O'BRIEN, J., ROWE, R., GADACZ, T., AND PALM, E. 1993. Interactively deformable models for surgery simulation. *IEEE Comput. Graphics & Applicat. 13,* 6 (Nov.), 68–75.

CROUCH, J. AND CHERRY, A. 2007. Parametric eye models. In *Medicine meets virtual reality*, J. Westwood, R. Haluck, H. Hoffman, G. Mogel, R. Phillips, R. Robb, and K. Vosburgh, Eds. Vol. 15. 91–93.

CROUCH, J., PIZER, S., CHANEY, E., HU, Y.-C., MAGERAS, G., AND ZAIDER, M. 2007. Automated finite element analysis for deformable registration of prostate images. *IEEE Trans. on Med. Imag. 26,* 10 (Oct.), 1379–1390.

DICK, C., GEORGII, J., AND WESTERMANN, R. 2011a. A hexahedral multigrid approach for simulating cuts in deformable objects. *IEEE Trans. on Visualization and Computer Graphics 17,* 11 (Nov.), 1663–1675.

DICK, C., GEORGII, J., AND WESTERMANN, R. 2011b. A real-time multigrid finite hexahedra method for elasticity simulation using CUDA. *Simulation Modelling Practice & Theory 19,* 2, 801–816.

DIMAIO, S.P.; SALCUDEAN, S. 2003. Needle insertion modeling and simulation. *IEEE Trans. on Robot. Autom. 19,* 5 (Oct.), 864–875.

DIMAIO, S. P. AND SALCUDEAN, S. E. 2002. Simulated interactive needle insertion. In *Proc. IEEE Symp. Haptic Interfaces Virtual Env. Teleoperator Syst.* 344.

DOBRIAN, F. AND POTHEN, A. 2006. Oblio: Design and performance. In *Applied Parallel Computing. State of the Art in Scientific Computing*, J. Dongarra, K. Madsen, and J. Wasniewski, Eds. Lecture Notes in Computer Science, vol. 3732. Springer Berlin Heidelberg, 758–767.

FOREST, C., DELINGETTE, H., AND AYACHE, N. 2002. Cutting simulation of manifold volumetric meshes. In *Proc. of Int. Conf. Medical Image Computing and Computer-Assisted Intervention, Part II*. Springer-Verlag, London, UK, 235–244.

FRANK, A. O., TWOMBLY, I. A., BARTH, T. J., AND SMITH, J. D. 2001. Finite element methods for real-time haptic feedback of soft-tissue models in virtual reality simulators. In *Proc. of IEEE Virtual Reality*. 257.

FUNG, Y. 1993. *Biomechanics: Mechanical Properties of Living Tissues*. Springer-Verlag.

GEFEN, A., SHALOM, R., ELAD, D., AND MANDEL, Y. 2009. Biomechanical analysis of the keratoconic cornea. *Journal of the mechanical behavior of biomedical materials 2,* 3, 224–236.

GEORGII, J. AND WESTERMANN, R. 2006. A multigrid framework for real-time simulation of deformable bodies. *Comput. & Graph. 30,* 3, 408–415.

GILBERT, J. 1994. Predicting structure in sparse matrix computations. *SIAM J. Matrix Anal. Appl. 15,* 1, 62–79.

GOKSEL, O. AND SALCUDEAN, S. 2011. Image-based variational meshing. *IEEE Trans. on Medical Imaging 30,* 1 (Jan.), 11–21.

HAGER, W. W. 1989. Updating the inverse of a matrix. *SIAM Rev. 31,* 2, 221–239.

HECHT, F., LEE, Y. J., SHEWCHUK, J. R., AND O'BRIEN, J. F. 2012. Updated Sparse Cholesky Factors for Corotational Elastodynamics. *ACM Trans. on Graphics 31*, 1–13.

HENG, P.-A., CHENG, C.-Y., WONG, T.-T., XU, Y., CHUI, Y.-P., CHAN, K.-M., AND TSO, S.-K. 2004. A virtual-reality training system for knee arthroscopic surgery. *IEEE Trans. on Information Technology in Biomedicine 8,* 2 (June), 217–227.

JAHYA, A., SCHOUTEN, M. G., FÜTTERER, J. J., AND MISRA, S. 2014. On the importance of modelling organ geometry and boundary conditions for predicting three-dimensional prostate deformation. *Computer methods in biomechanics and biomedical engineering 17,* 5, 497–506.

JAMES, D. L. AND PAI, D. K. 1999. Artdefo: accurate real time deformable objects. In *Proc. of ACM SIGGRAPH*. 65–72.

JAMES, D. L. AND PAI, D. K. 2003. Multiresolution Green's function methods for interactive simulation of large-scale elastostatic objects. *ACM Trans. on Graphics 22*, 47–82.

JOLDES, G. R., WITTEK, A., AND MILLER, K. 2009. Suite of finite element algorithms for accurate computation of soft tissue deformation for surgical simulation. *Medical Image Analysis 13,* 6, 912–919.

JOLDES, G. R., WITTEK, A., AND MILLER, K. 2010. Real-time nonlinear finite element computations on GPU applications to neurosurgical simulation. *Computer Methods on Applied Mechanics and Engineering 199,* 4952, 3305–3314.

JUSZCZYK, M. M., CRISTOFOLINI, L., AND VICECONTI, M. 2011. The human proximal femur behaves linearly elastic up to failure under physiological loading conditions. *Journal of biomechanics 44,* 12, 2259–2266.

KEAVENY, T. M., GUO, X. E., WACHTEL, E. F., MCMAHON, T. A., AND HAYES, W. C. 1994. Trabecular bone exhibits fully linear elastic behavior and yields at low strains. *Journal of biomechanics 27,* 9, 1127–1136.

KOÇAK, U., PALMERIUS, K. L., AND COOPER, M. 2009. Dynamic deformation using adaptable, linked asynchronous FEM regions. In *Proc. of ACM Spring Conf. Comput. Graph.* 197–204.

LAPEER, R., GASSON, P., AND KARRI, V. 2010. Simulating plastic surgery: From human skin tensile tests, through hyperelastic finite element models to real-time haptics. *Progress in Biophysics & Molecular Biology 103,* 23, 208–216.

LEDERMAN, C., JOSHI, A., DINOV, I., VAN HORN, J., VESE, L., AND TOGA, A. 2010. Tetrahedral mesh generation for medical images with multiple regions using active surfaces. In *IEEE Int. Symp. Biomedical Imaging: From Nano to Macro*. 436–439.

LEE, B., POPESCU, D. C., AND OURSELIN, S. 2010. Topology modification for surgical simulation using precomputed finite element models based on linear elasticity. *Progress in Biophysics & Molecular Biology 103,* 23, 236–251.

LINDBLAD, A. AND TURKIYYAH, G. 2007. A physically-based framework for real-time haptic cutting and interaction with 3d continuum models. In *Proc. of ACM Symp. Solid & Physical Modeling*. 421–429.

LIPTON, R. J., ROSE, D. J., AND TARJAN, R. E. 1979. Generalized nested dissection. *SIAM J. Numer. Anal. 16,* 2 (Apr.), 346–358.

LIU, J. W. H. 1990. The role of elimination trees in sparse factorization. *SIAM J. Matrix Anal. Appl. 11,* 1, 134–172.

MARCHESSEAU, S., HEIMANN, T., CHATELIN, S., WILLINGER, R., AND DELINGETTE, H. 2010. Fast porous visco-hyperelastic soft tissue model for surgery simulation: Application to liver surgery. *Progress in Biophysics & Molecular Biology 103,* 23, 185–196.

MIKIELEWICZ, M., MICHAEL, R., MONTENEGRO, G., PINILLA CORTES, L., AND BARRAQUER, R. 2013. Elastic properties of human lens zonules as a function of age in presbyopes. *Acta Ophthalmologica 91,* s252, 0–0.

MOHAMED, A. AND DAVATZIKOS, C. 2004. Finite element mesh generation and remeshing from segmented medical images. In *IEEE Int. Symp. Biomedical Imaging: Nano to Macro*. Vol. 1. 420–423.

MOR, A. AND KANADE, T. 2000. Modifying soft tissue models: Progressive cutting with minimal new element creation. In *Medical Image Computing and Computer-Assisted Intervention*, S. Delp, A. DiGoia, and B. Jaramaz, Eds. Lecture Notes in Computer Science, vol. 1935. Springer Berlin / Heidelberg, CH412–CH412.

MOS, N., DOLBOW, J., AND BELYTSCHKO, T. 1999. A finite element method for crack growth without remeshing. *Int. J. for Numerical Methods in Engineering 46,* 1, 131–150.

NIENHUYS, H.-W. AND VAN DER STAPPEN, A. F. 2001. A surgery simulation supporting cuts and finite element deformation. In *Proc. 4th Int. Conf. Medical Image Computing and Computer-Assisted Intervention*. Springer-Verlag, London, UK, 145–152.

NIKITIN, I., NIKITINA, L., FROLOV, P., GOEBBELS, G., GÖBEL, M., KLIMENKO, S., AND NIELSON, G. M. 2002. Real-time simulation of elastic objects in virtual environments using finite element method and precomputed Green's functions. In *Proc. of Eurographics Workshop on Virtual Environments*. 47–52.

NVIDIA. 2013. CUDA Toolkit 5.0 performance report.

PICINBONO, G., LOMBARDO, J.-C., DELINGETTE, H., AND AYACHE, N. 2002. Improving realism of a surgery simulator: linear anisotropic elasticity, complex interactions and force extrapolation. *J. for Vis. Comput. Animat. 13,* 3, 147–167.

SEDEF, M., SAMUR, E., AND BASDOGAN, C. 2006. Real-time finite-element simulation of linear viscoelastic tissue behavior based on experimental data. *IEEE Comput. Graph. Appl. 26,* 6 (Nov.-Dec.), 58–68.

SELA, G., SUBAG, J., LINDBLAD, A., ALBOCHER, D., SCHEIN, S., AND ELBER, G. 2007. Real-time haptic incision simulation using FEM-based discontinuous free-form deformation. *Computer Aided Design 39,* 8, 685–693.

SERBY, D., HARDERS, M., AND SZÉKELY, G. 2001. A new approach to cutting into finite element models. In *Proc. of the 4th Int. Conf. Medical Image Computing & Computer-Assisted Intervention*. Springer-Verlag, London, UK, 425–433.

SPILLMANN, J. AND HARDERS, M. 2012. Robust interactive collision handling between tools and thin volumetric objects. *IEEE Trans. on Visualization and Computer Graphics 18,* 8 (Aug.), 1241–1254.

STEINEMANN, D., HARDERS, M., GROSS, M., AND SZEKELY, G. 2006. Hybrid cutting of deformable solids. In *Prof. of IEEE Virtual Reality*. 35–42.

TERZOPOULOS, D. AND FLEISCHER, K. 1988. Modeling inelastic deformation: viscolelasticity, plasticity, fracture. *SIGGRAPH Computer Graphics 22,* 4 (June), 269–278.

TERZOPOULOS, D., PLATT, J., BARR, A., AND FLEISCHER, K. 1987. Elastically deformable models. *SIGGRAPH Computer Graphics 21,* 4 (Aug.), 205–214.

TESCHNER, M., KIMMERLE, S., HEIDELBERGER, B., ZACHMANN, G., RAGHUPATHI, L., FUHRMANN, A., CANI, M.-P., FAURE, F., MAGNENAT-THALMANN, N., STRASSER, W., AND VOLINO, P. 2005. Collision detection for deformable objects. *Computer Graphics Forum 24,* 1, 61–81.

TURK, G. AND LEVOY, M. 1994. Zippered polygon meshes from range images. In *Proc. of ACM SIGGRAPH*. 311–318.

TURKIYYAH, G. M., KARAM, W. B., AJAMI, Z., AND NASRI, A. 2011. Mesh cutting during real-time physical simulation. *Computer Aided Design 43,* 7 (July), 809–819.

VIGNERON, L. M., VERLY, J. G., AND WARFIELD, S. K. 2004. Modelling surgical cuts, retractions, and resections via extended finite element method. In *Proc. of the 7th Int. Conf. Medical Image Computing and Computer-Assisted Intervention, Part II*, C. Barillot, D. R. Haynor, and P. Hellier, Eds. Lecture Notes in Computer Science, vol. 3217. Springer, 311–318.

WITTEK, A., JOLDES, G., COUTON, M., WARFIELD, S. K., AND MILLER, K. 2010. Patient-specific non-linear finite element modelling for predicting soft organ deformation in real-time; application to non-rigid neuroimage registration. *Progress in Biophysics & Molecular Biology 103,* 23, 292–303.

WU, W. AND HENG, P. A. 2004. A hybrid condensed finite element model with GPU acceleration for interactive 3d soft tissue cutting: Research articles. *Comput. Animat. Virtual Worlds 15,* 3-4, 219–227.

WU, W. AND HENG, P. A. 2005. An improved scheme of an interactive finite element model for 3d soft-tissue cutting and deformation. *The Visual Computer 21*, 707–716.

WU, X., DOWNES, M. S., GOKTEKIN, T., AND TENDICK, F. 2001. Adaptive nonlinear finite elements for deformable body simulation using dynamic progressive meshes. In *Proc. of Eurographics*, A. Chalmers and T.-M. Rhyne, Eds. Vol. 20(3). Blackwell Publishing, 349–358.

WU, X. AND TENDICK, F. 2004. Multigrid integration for interactive deformable body simulation. In *Medical Simulation*, S. Cotin and D. Metaxas, Eds. Lecture Notes in Computer Science, vol. 3078. Springer Berlin / Heidelberg, 92–104.

ZHANG, X. AND KIM, Y. 2012. Simple culling methods for continuous collision detection of deforming triangles. *IEEE Trans. on Visualization and Computer Graphics 18,* 7 (July), 1146–1155.

ZHONG, H., WACHOWIAK, M. P., AND PETERS, T. M. 2005. Adaptive finite element technique for cutting in surgical simulation. *Medical Imaging 2005: Visualization, Image-Guided Procedures, and Display 5744,* 1, 604–611.

ZHU, Y., SIFAKIS, E., TERAN, J., AND BRANDT, A. 2010. An efficient multigrid method for the simulation of high-resolution elastic solids. *ACM Trans. on Graphics 29,* 2 (Apr.), 16:1–16:18.

Received April 2014; accepted December 2015

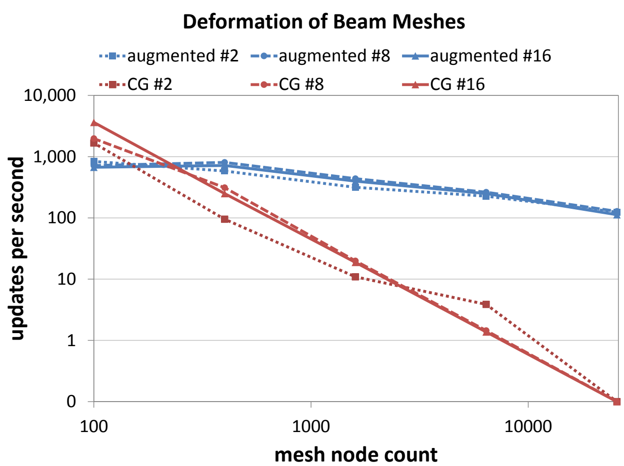

(a)

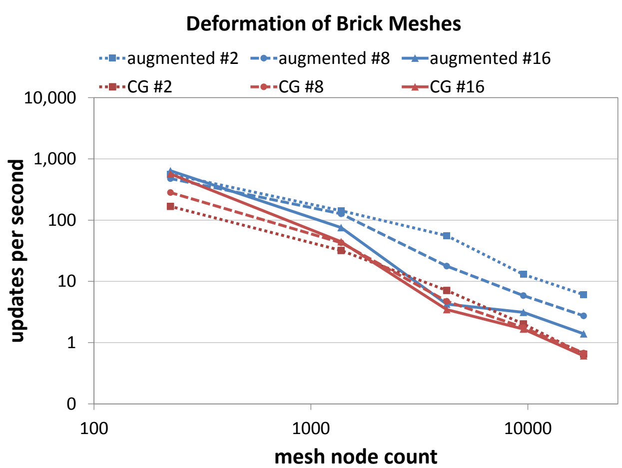

(b)

Fig. 6: Update rates are shown for the series of (a) beam and (b) brick meshes. CG results are shown with red lines, and augmented method results are shown with blue lines. Dotted lines show the results for deformation step #2 across the series of test mesh sizes. Dashed lines show results for deformation step #8, and solid lines for deformation step #16.

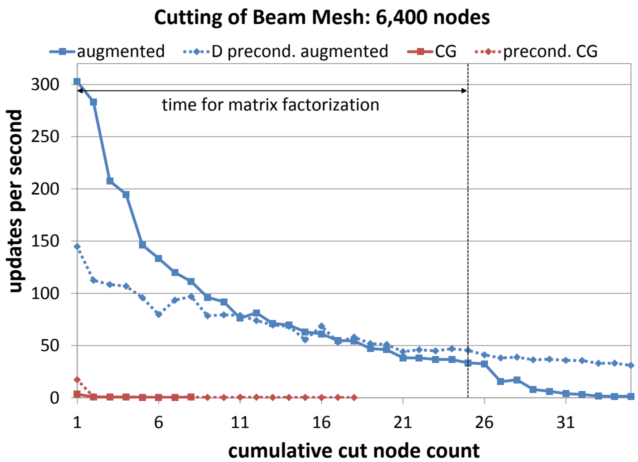

(a)

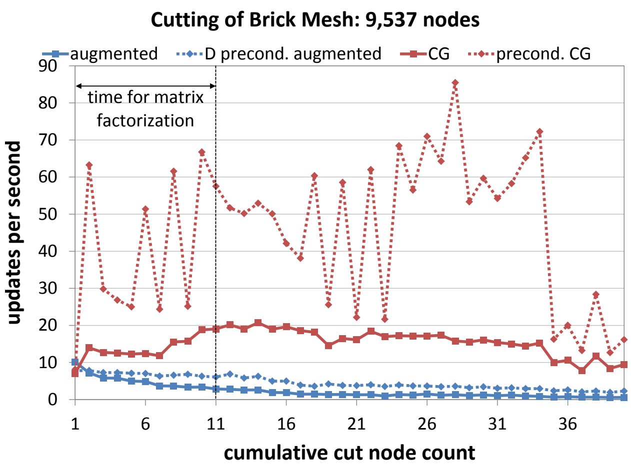

(b)

Fig. 7: Update rates are shown for the augmented and CG methods as a cut is advanced through a (a) beam mesh and (b) brick mesh.

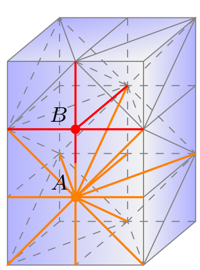

Fig. 8: A portion of the tetrahedral brick test mesh. Node A has 13 connected nodes (colored in orange) whereas Node B only has 5 (colored in red).

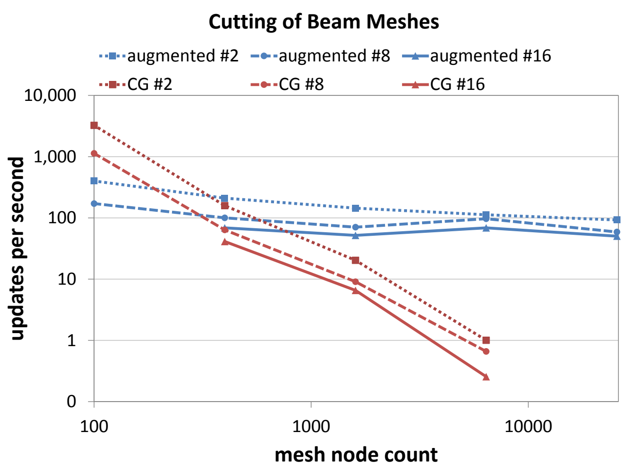

(a)

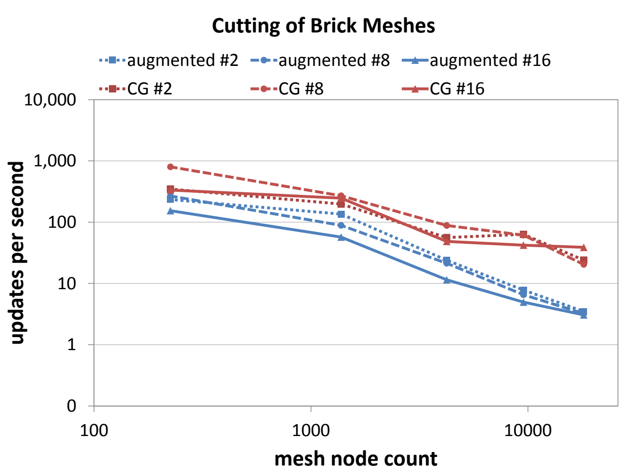

(b)

Fig. 9: Update rates are shown for the series of (a) beam and (b) brick meshes. CG results are shown with red lines, and augmented method results are shown with blue lines. Dotted lines show the results for cutting step #2 across the series of test mesh sizes. Dashed lines show results for cutting step #8, and solid lines for cutting step #16.

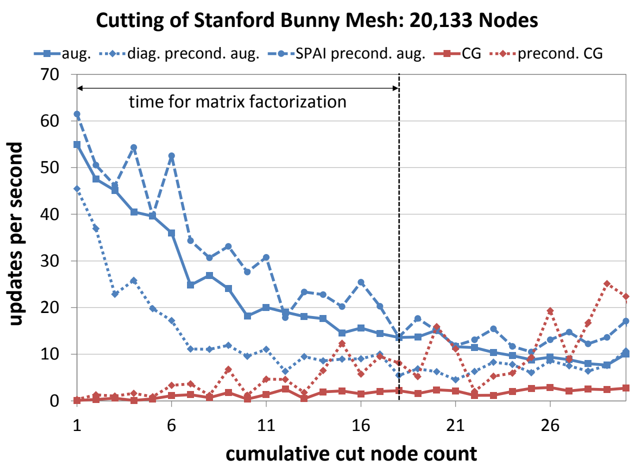

(a)

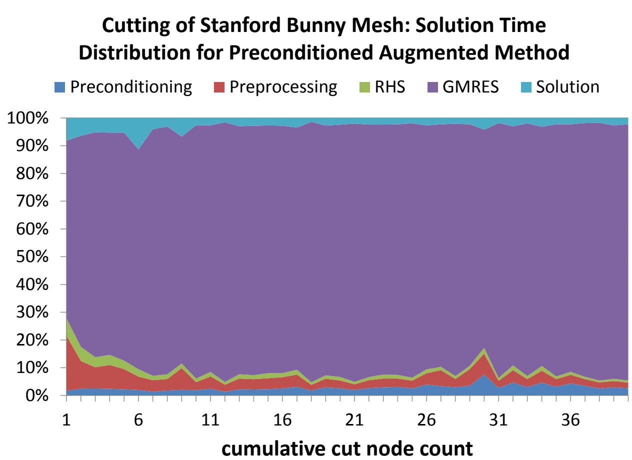

(b)

Fig. 10: Timing results are provided for the bunny mesh cutting experiment. (a) Update rates are shown for the augmented and CG methods as a cut is advanced. (b) The allocation of computation time to steps of the augmented method is shown.

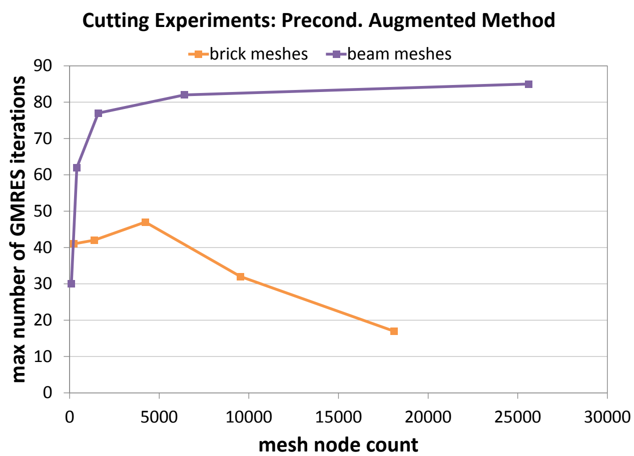

(a)

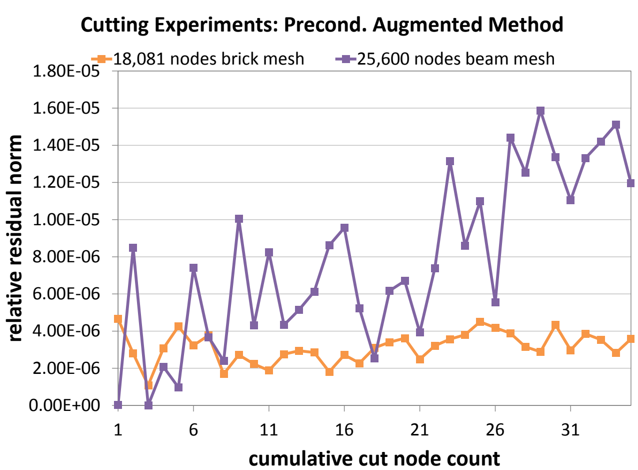

(b)

Fig. 11: (a) The maximum number of GMRES iterations required by the beam and brick meshes of a specific size. (b) Relative residual norm vs. cut depth. For a solution $\hat{x}$ to the system $Ax = b$, relative residual norm is defined as $\|A\hat{x} - b\|_2 / \|b\|_2$.

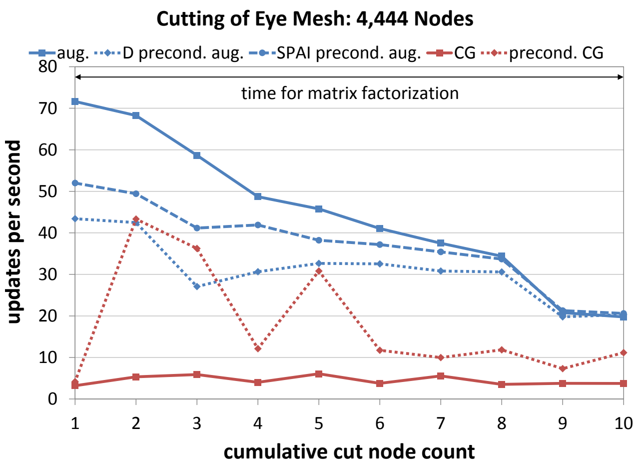

(a)

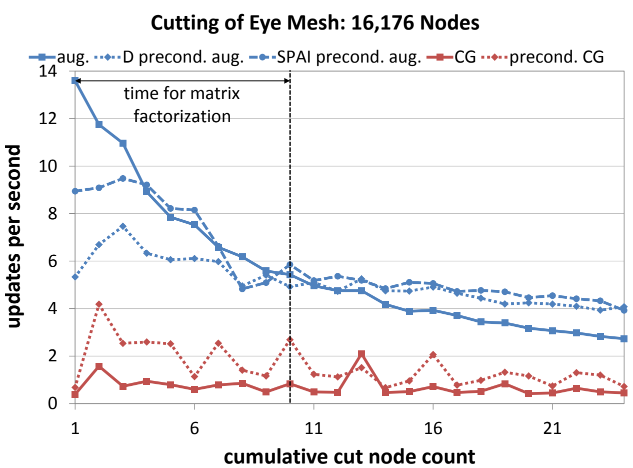

(b)

Fig. 12: Timing results are provided for the eye meshes of (a) 4,444 nodes and (b) 16,176 nodes.

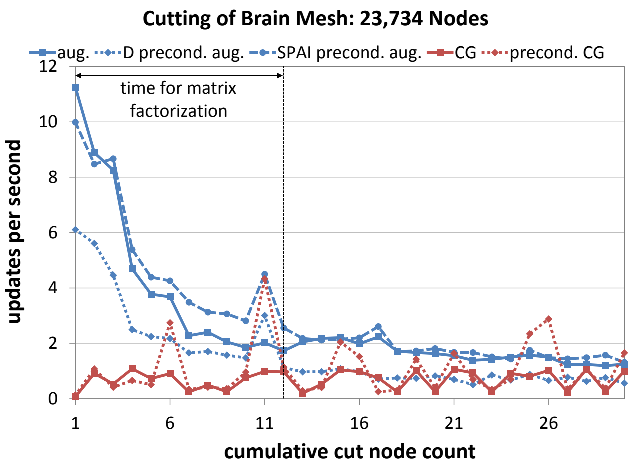

(a)

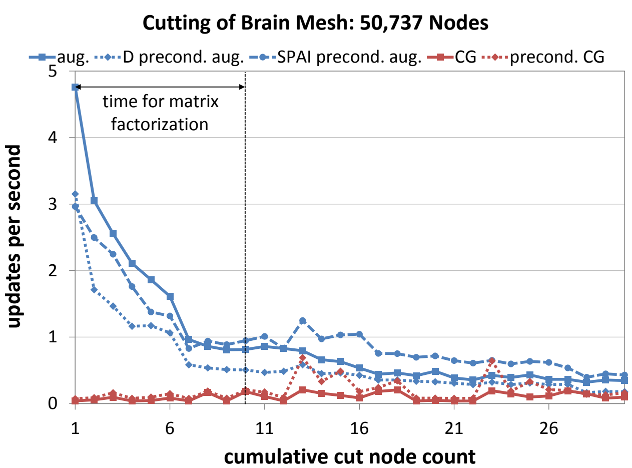

(b)

Fig. 13: Timing results are provided for the brain meshes of (a) 23,734 nodes and (b) 50,737 nodes.